Journal of Energy Storage 89 (2024) 111709

Contents lists available at ScienceDirect

Journal of Energy Storage

journal homepage: www.elsevier.com/locate/est

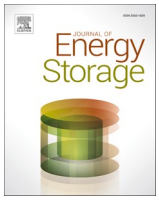

Research papers

Effect of steam flow parameters on the partial load behaviour of a PCM storage

Larissa Dietz *, Inga Bürger, Andrea Gutierrez

Institute of Engineering Thermodynamics, German Aerospace Center (DLR), Pfaffenwaldring 38-40, 70569 Stuttgart, Germany

ARTICLE INFO

Keywords:
Phase change material
Thermal storage
Partial load operating strategies
Steam generation
Numerical study
Analytical description

ABSTRACT

To estimate the achievable thermal power in passive latent heat thermal energy storage (LH-TES) systems and the corresponding charging/discharging times for customised storage design and operation, relevant influencing parameters and their impact must be sufficiently known and understood. These parameters include not only the well-researched parameters on the phase change material (PCM) side, but also the parameters on the heat transfer fluid (HTF) side, such as the inlet temperature, the mass flow rate and the resulting heat transfer coefficient (HTC) between the HTF flow and the tube wall. For heat exchangers, these influences have been studied well, however for highly transient LH-TES studies are scarce. This article presents the influence of relevant parameters focusing on the ones related to the HTF side, using analytical and numerical parameter studies in Matlab®. The effect of different HTCs for varying flow conditions of the HTF in different zones of the tube is utilised to introduce the *dominant heat transfer surface between the storage and the HTF (DHTS)* as an indirect operating parameter. It corresponds to the area where the HTF phase change occurs and where most of the total energy is transferred. The numerical study indicates that the size of the dominant heat transfer area and thus the DHTS can be adapted by the HTF mass flow rate and the temperature difference between the HTF inlet temperature and the PCM phase change temperature. Based on this knowledge, new conjugate design and operating strategies for a test rig with a nominal thermal power of 1 kW using the commercial PCM PLUSICE A133 as storage material are proposed. They lead to a peak shaving behaviour of the storage with defined charging and discharging times.

1. Introduction

Thermal energy storage systems are a key technology for the efficient use of energy resources, the decoupling of renewable energy supply from energy demand and increasing the reliability of energy systems. They are used in heating and cooling applications as well as in power plants and process industry. Besides sensible and thermochemical heat storages, latent heat thermal energy storages (LH-TES) offer high energy densities and high exergetic efficiency [1]. In the field of latent heat storage, the shell and tube type is popular due to its simple design [2]. The performance of this type of storage and especially its peak thermal power is limited by a variety of phase change material (PCM)-side and heat transfer fluid (HTF)-side system-specific influencing parameters.

A detailed review of LH-TES in tube-and-shell design with a focus on PCM for medium and high-temperature applications by Li et al. [2] shows that research in this field mainly focuses on the PCM side of systems and on single-phase HTFs. They include analytical, numerical and experimental thermal power studies on the effect of geometric, PCM-side and HTF-side parameters. Eleven out of sixteen publications in this review focus on the PCM side (e.g. [3,4]). Also measures to enhance the thermal power of LH-TES in tube-and-shell design on the PCM side, as fins and extended surfaces (e.g. [5,6]), employment of PCM cascades (e.g. [7,8]), impregnation of porous matrixes and the use of form-stable composite salts (e.g. [9,10]), are thoroughly discussed by several authors on nearly 16 pages. Enhancement techniques on the HTF side on the other hand, as grooved, dimpled and finned tubes (e.g. [9,11,12]), the variation of the inlet temperature and mass flow rate as well as the addition of nanoparticles (e.g. [13]), are presented on a single page.

However, there are studies that deal with the research question of the coupled heat transfer between PCM and HTF in LH-TES with a single-phase fluid. Cao et al. numerically correlate the heat transfer, including the PCM phase change and forced convection, in a double tube configuration [14]. They state that the 2D velocity field of the flow reaches a steady state quickly, while the temperature field keeps on changing with the progressing melting interface. Bellecci [15] then

* Corresponding author.
E-mail address: larissa.dietz@dlr.de (L. Dietz).

https://doi.org/10.1016/j.est.2024.111709
Received 14 July 2023; Received in revised form 9 April 2024; Accepted 15 April 2024
Available online 22 April 2024

Nomenclature

Latin

a	analytical
a_{PCZ}	HTF phase change zone in tube (m^2)
A	area (m^2)
b	volumetric fin fraction
c	charging
c_p	specific heat capacity (J/kg)
C_0	distribution coefficient drift flux model
d	discharging
d	diameter (m)
e	experimental
f	liquid fraction of PCM
G	mass flux ($kg/(sm^2)$)
h	specific enthalpy (J/kg)
$h_{HTF/w}$	heat transfer coefficient between HTF and wall ($W/(m^2K)$)
Δh	phase change enthalpy (J/kg)
j	volume flux in drift flux model (m/s)
L	length (m)
DHTS	dominant heat transfer surface between storage and HTF
$\dot{m}$	mass flow rate (g/s)
n	numerical
Nu_t	Nusselt number, turbulent
p	pressure (Pa)
Pr	Prandtl number
$\dot{q}$	heat flux (W/m^2)
$\dot{Q}$	thermal power (W)
r	radius (m)
r, z	r-, z-coordinates (m)
Re	Reynolds number
s	layer thickness (m)
S	source term in energy eq. (W/m^3)
t	time (s)
T	temperature (K)
$v_{HTF,vap,j}$	drift velocity in drift flux model (m/s)
V	volume (m^3)
x	steam fraction

Greek

α	void fraction
δ	condensation film thickness (m)
Δ	difference
λ	thermal conductivity (W/(mK))
ρ	density (kg/m^3)

Subscripts

A	acceleration
b	boundary
B	boiling
C	condensation
eff	effective
F	friction
FC	forced convection
g	gaseous
G	gravity
H	homogeneous
i	inner
in	inlet
l	liquid
lg	liquid/gaseous
liq	liquidus
max	maximum
min	minimum
o	outer
out	outlet
pc	phase change
radial	in radial direction
s	solid
sl	solid/liquid
sol	solidus
stor	storage
w	tube wall

Abbreviations

1p	single-phase
2p	two-phase
HDPE	high-density polyethylene
HTC	heat transfer coefficient
HTE	heat transfer enhancement
HTF	heat transfer fluid
HTR	heat transfer resistance
LH-TES	latent heat thermal energy storage
PCM	phase change material
PVC	polyvinyl chloride

simplified this approach by modelling the forced convection heat transfer by empirical correlations assuming steady-state HTCs and thus treating the fluid velocity as an independent variable. Lacroix [16] developed a theoretical model aiming to predict the transient melting behaviour of the PCM in a tube-and-shell storage unit. His parameter studies reveal that radii of the shell, HTF mass flow rates and HTF inlet temperatures have to be chosen carefully for performance optimisation. Zhang et al. [17] solved the melting process of a PCM in a thermal energy storage system with laminar forced convection water flow, using a conjugate semi-analytical model and discussed the need for conjugate analysis of phase change and flow. They showed that laminar forced convective heat transfer for fluids with moderate Prandtl numbers must be treated coupled with the PCM phase change. Trp et al. [18] reached the same conclusion and Ismail et al. [19] numerically showed that higher Reynolds numbers and Stefan numbers result in a faster melting process. Furthermore, Zauner et al. [20] derived power control options from their observations and described the HTF mass flow rate as a main control variable. This is confirmed by Wang et al. [21] and Niyas et al. [22]. Also, very recent results published in 2023 by Bahlekeh et al. [23] and Chatroudi et al. [24] numerically show the effects of the fin geometry in the PCM as well as of the Reynolds number in the HTF flow on the solidification power respectively on the melting process. Thus, while these studies suggest that a conjugate approach is required, it is indicated that a significant effect of the HTF on the overall performance is not apparent in all conditions.

This is confirmed by several studies indicating that there are limited or neglectable HTF-side effects on the storage performance for single-phase HTF operation. E.g., Murray et al. [25] state that effects due to HTF mass flow rate variations occur only when a part of the initially solid PCM has already melted. In the case of the discharging, a rise in the mass flow rate has no effect on the solidification time. Sari et al. [26] experimentally proved that melting and solidification times in the tested laminar range are not affected by the flow rate of the HTF, which is confirmed by experimental results conducted by Hasan [27], as well as Akgün et al. [28] showing experimentally that the Reynolds number of the HTF does not have a considerable effect on the total melting time.

The influence of HTF and PCM on the thermal power of two-phase HTF LH-TES systems has so far only been investigated on two test rigs

known to the best of our knowledge. Laing et al. published the experimental results of an LH-TES unit integrated into a solar thermal power plant with direct steam generation and tested it in different operating modes [29–31]. The evaporator is operated at full load, implying that the entire inner tube surface is used for HTF phase change. Nevertheless, a fluctuating water column level occurs in the tubes at the beginning of the discharging process, which is detected by thermocouples measuring the PCM temperature and the tube wall temperature simultaneously. In the zones where the PCM temperature is equal to the tube wall temperature, a single-phase flow is expected, leading to a higher thermal resistance between HTF and tube wall compared to that between PCM and tube wall. These observations confirm that the HTC can, for specific times and locally, limit the thermal power of the storage. Garcia et al. experimentally studied an LH-TES unit for concentrating solar power plants at the LHASSA test facility in once-through operation and validated numerical design models first for full-load operation [32,33] and later for advanced operating strategies [34]. These advanced strategies included the demonstration of a stable HTF mass flow rate and thus constant thermal power at constant pressure by gradually increasing the liquid water level in the tubes during discharging to take advantage of the increasing heat exchanger surface. This operating strategy was called partial load operation and indicated an effect of the HTF condition on the overall LH-TES performance. On the simulation side, this finding was accounted for by Beust et al. [35] who improved the corresponding model by additionally considering a local HTC on the HTF-side of the tube in charging operation. Furthermore, Johnson et al. [36] published a model and simulation results for the design of an LH-TES for steam generation in full load, and Vogel et al. [37] for partial load operation. Table 1 summarises the characteristic properties of the above-introduced investigations.

To summarise, numerous studies have reported specific LH-TES units analytically, numerically and/or experimentally. However, in the previous studies inconsistent conclusions about the relevance of the PCM-side and the HTF-side thermal resistance for the overall heat transfer and thus also for the peak thermal power of LH-TES were met. Furthermore, the majority of investigations were done on single-phase HTF systems.

This article aims to fill this research gap by incorporating the HTF-side parameters and methods to control thermal power in LH-TES for more sophisticated conclusions when analysing two-phase HTF systems. For this, the interaction of transient influencing parameters and their effect on the thermal power is analytically investigated. Besides the well-researched heat transfer resistance of the PCM, the HTC as well as the mass flow rate of the HTF are included in the analysis. Furthermore, the importance of an indirect thermal power operating parameter, the dominant heat transfer surface (DHTS), is introduced and it is demonstrated numerically how its size in the tube can be adjusted by the HTF settings and how this affects the resulting thermal power of the storage. Finally, these new findings are taken into account in existing strategies for storage design and operation. Thus, solutions for peak shaved thermal power profiles with defined charging and discharging times and axial charging/discharging behaviour can be proposed. This capability to precisely control the thermal power of the storage, is key to the implementation of LH-TES in the industry.

The analytical model and the numerical model are described in the methodology chapter in Section 2. Corresponding parameter studies are presented in Section 3 and discussed in Section 4.

2. Methodology

Two different models, implemented in Matlab®, are used to investigate the effects of parameter variations on the thermal power of the storage. The purpose of the analytical model, which is described for the first time in Section 2.1, is to determine the interaction of the two transient radial heat transfer resistances regarding the thermal power of the storage: The distance between the outer tube wall and the phase change boundary on the one-hand and the HTC on the other. A particular focus is on determining thresholds for the transition from PCM-side limited operation to HTF-side limited operation. Furthermore, the options for adjusting an indirect operating parameter, the *dominant heat transfer surface (DHTS)*, are discussed based on an HTF mass flow rate study. Section 2.2 describes the numerical study, which shows in more detail how the DHTS can be set using the conventional HTF operating parameters, more specifically the HTF mass flow rate and the HTF inlet temperature, and how this affects the thermal power of the storage. The numerical model used for this was developed at DLR by Vogel et al. and is described in [37]. Based on the results, a combination of design approaches and optimised operating strategies with a focus on the HTF parameters is discussed.

2.1. Analytical model

This chapter introduces the analytical model developed by the authors of this study. It is based on systematic assumptions to reduce the complexity of the fin geometry and transient effects. Due to its simplification, it is not suitable for the actual design of a storage element, but it is sufficient to illustrate schematically how the represented parameters tend to influence the thermal power of the storage. This helps to introduce an indirect operating parameter, the DHTS, and to show generically in which cases it can be effectively controlled by the HTF mass flow rate. In Section 2.1.1., the simulated geometry is described. Subsequently, assumptions are made and limitations are pointed out in Section 2.1.2, followed by the mathematical formulation of the model in Section 2.1.3.

Table 1
Characteristic properties of the investigations introduced in Section 1. The investigation methods are either analytical (a), numerical (n) or experimental (e), the HTFs are either single-phase (1p) or two-phase (2p), the outer HTF tube diameter is d, the heat enhancement measure is HTE, some properties are not specified (n. s.).

	a/n/e	PCM	HTF	tube material	d (m)	HTE
[15]	n	Lithium fluoride	Air (1p)	n. s.	n. s.	–
[16]	n,e	n-Octadecane	Water (1p)	Copper	0.0158	–
[17]	a	n-Octadecane	Water (1p)	High conductivity metal	n. s.	–
[18]	n/e	Rubitherm RT 30	Water (1p)	Copper	0.035	–
[19]	n	n. s.	n. s. (1p)	n. s.	n. s.	–
[20]	e	HDPE	Marlotherm SH (1p)	Steel 1.0345	n. s.	Aluminium alloy fins
[21]	e	Erythritol	Air (1p)	Stainless steel 304	0.108	–
[22]	e	Potassium nitrate, sodium nitrate, sodium nitrite 53:7:40	Hi-Tech Therm 60 (1p)	Copper	0.0127	Copper fins
[25]	e	Dodecanoic acid, lauric acid	Water (1p)	Copper	0.0127	Copper fins
[26]	e	Stearic acid	Water (1p)	Copper	0.05	–
[27]	e	Palmitic acid	Water (1p)	PVC	0.11	–
[28]	e	P42–44, P46–48 P56–58 (Merck)	Water (1p)	Copper	0.028	–
[29–31]	e	Sodium nitrate	Water (2p)	Steel	0.0213	Aluminium fins
[32–34]	e	Sodium nitrate	Water (2p)	Steel	n. s.	Aluminium fins

2.1.1. Geometry described by the analytical model

The model represents the symmetric part of the longitudinal section of a finned tube in a tube-and-shell design LH-TES, as shown in Fig. 1, in this case during discharging. The r-axis represents the radial dimension, starting from the symmetry axis of the tube on the left-hand side. On the z-axis, the length of the HTF tube L is depicted. The tube wall, restricted by the inner and the outer diameter r_i and r_o, separates the HTF (in light blue) on the left and the storage, consisting of the PCM and the fins (in brown and light brown), on the right. While the HTF is flowing through the tube, the storage remains passive in the container. Temperature, mass flow rate and pressure are referred to as T_{HTF}, $\dot{m}_{HTF}$ and p_{HTF} respectively. In the model, they are assumed to be constant over the entire tube length. The phase change temperature of the PCM is $T_{PCM,pc}$. The radial dimensions of the HTF flow, the HTF tube, the solid storage layer and the liquid storage layer are labelled as s_{HTF}, s_w, $s_{stor,s}$ and $s_{stor,l}$ respectively. To characterise the condition of the two-phase HTF, $x_{HTF,in(z=0)}$ indicates the steam fraction at the inlet of the tube, while $x_{HTF,out\ (z=L)}$ indicates the steam fraction at the outlet. Furthermore, relevant heat transfer properties are the HTC between the HTF and the tube wall $h_{HTF/w}$ and the thermal conductivities of the tube wall λ_w as well as of the solid and the liquid storage $\lambda_{eff,s}$ and $\lambda_{eff,l}$.

2.1.2. Assumptions for the analytical model

The analytical model is based on the following assumptions:

1) Steady-state: Only one point of time is represented, which results in a constant distance between the outer tube wall and the phase change boundary of the PCM in the storage; $s_{stor,s} = \text{const.}$
2) Phase change occurs on the inner side of the tube (in the HTF) and on the outer side of the tube (in the storage), resulting in a constant temperature difference between PCM and HTF over the entire tube length; $\Delta T = \text{const.}$
3) Isothermal HTF flow: The HTF leaves the tube at inlet temperature; $T_{HTF,in} = T_{HTF,out} = T_{HTF}$.
4) A constant HTC between HTF and the inner tube wall is assumed.
5) There is no natural convection in the storage.
6) The storage material (PCM/fins) is homogeneous, its conductivity is calculated as shown in Eq. (3).
7) The thermal conductivity of the PCM equals the arithmetic mean value over the relevant temperature range either for the solid (during discharging) or the liquid (during charging) PCM.
8) There is no thermal resistance between the effective storage material and the outer tube wall.

Assuming this, the analytical model neglects the temporal and spatial transience of the phase change process and simplifies the mathematical formulation of the heat transfer. The results of the model are therefore used to analyse individual points in time and individual positions in the LH-TES to derive trends and understand the relationships between the influencing variables.

2.1.3. Mathematical formulation of the analytical model

In the analytical model, two different thermal powers are calculated independently, which represent the theoretical maximum values. Firstly, there is a maximum thermal power that can be absorbed or released by the HTF, assuming that the radial heat transfer resistance in the storage is zero. It is, considering the assumptions in Section 2.1.2,

$$\dot{H}_{HTF,out} - \dot{H}_{HTF,in} = \dot{H}_{HTF} = \dot{m}_{HTF}\Delta h_{HTF.} \tag{1}$$

Secondly, the maximum thermal power that can be transferred radially between the inner tube wall and the PCM phase change boundary is considered (see Eq. (2)), the potential limitation of the HTF side is neglected.

$$\dot{Q}_{radial} = \dot{q}_{radial} A_w = \frac{1}{\left\{\frac{1}{h_{HTF/w}}\right\}_1 + \left\{\frac{s_w}{\lambda_w}\right\}_2 + \left\{\frac{s_{PCM}}{\lambda_{PCM,eff}}\right\}_3} \frac{2\pi\left(\frac{d_o}{2} - \frac{d_i}{2}\right)L}{ln\left(\frac{d_o}{d_i}\right)} \left(T_{HTF} - T_{PCM,pc}\right) \tag{2}$$

The effective thermal conductivity of the PCM ($\lambda_{PCM,eff}$) in Eq. (2) is thereby defined as

$$\lambda_{PCM,eff} = (1-b)\lambda_{PCM} + b\lambda_{fins} \tag{3}$$

In Fig. 1, these thermal powers are represented by arrows. A look at Eqs. (1) and (2) indicates the influencing parameters for the thermal power of the storage. Firstly, they include the mass flow rate $\dot{m}_{HTF}$ as an operating parameter. Furthermore, there are parameters defined by the geometry of the setup, such as the heat transfer surface, depending on the inner and outer tube diameter r_i and r_o, the tube length L and the fin geometry described by the fin fraction b. The heat transfer resistance results from the thickness of the heat conducting layers s_w and s_{PCM} as well as the HTC $h_{HTF/w}$. Last, material properties, such as the thermal conductivity of the tube wall λ_w, of the fins λ_{fins} and of the PCM λ_{PCM}, the phase change temperature of the PCM $T_{PCM,pc}$ as well as the phase change temperature T_{HTF} and phase change enthalpy $\Delta h_{PCM,sl}$ of the HTF influence the thermal power in LH-TES.

The results for Eqs. (1) and (2) are calculated separately and

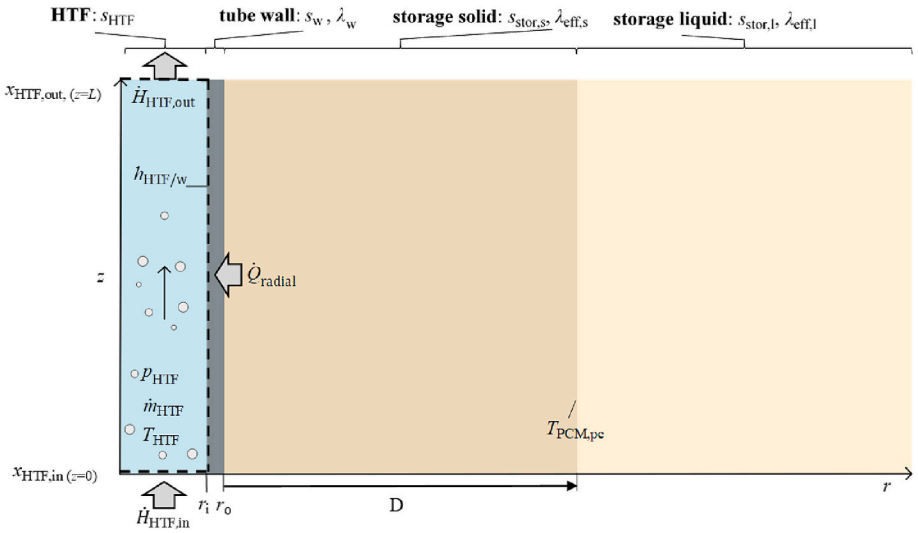

Fig. 1. Schematic of model geometry for the analytical model with heat transfer variables during discharging.

compared to identify boundary cases. The lower value represents the total thermal power of the storage.

2.2. Numerical model

The numerical model approximates the transient conjugate processes in the HTF and in the storage. It enables the simulation of operating modes where variable parts of the heat exchanger tubes are used for the phase change of the HTF and resolves the temperature field and the liquid fraction of the storage. Thus, the HTF-side operating condition and the formation of the phase change boundary in radial and axial directions can be correlated and linked to the corresponding thermal power characteristics. This DLR-intern numerical tool called FASTER (Fast and Adjustable Simulation of Thermal Energy stoRage), is developed by Vogel et al. and described in detail in [37] and will be outlined briefly below. The HTF part has been successfully validated using Apros®, a commercial software for modelling and dynamic simulation of energy systems, the results are documented in [37]. Furthermore, the PCM part has been calibrated using simulations of the cross-section of one tube, including PCM and aluminium fins, in Fluent®. Refining the final grid resulted in a maximum deviation of the heat flux of 1.4 %, of the liquid fraction of 0.0005 %, and of the average volumetric storage temperature of 0.09 %. The automatic region refinement in Fluent® reduced the size of the largest and the smallest cell in the grid, thereby from $3{\cdot}10^{-9}$ m^3 and 10^{-7} m^3 to $8{\cdot}10^{-10}$ m^3 and $3{\cdot}10^{-8}$ m^3. The final time step size is 5 s. In [37], the general calibration process is documented.

2.2.1. Geometry described by the numerical model

The model is divided into an HTF part and a storage part, where the latter consists of the PCM and the fins as in the analytical model. Fig. 2 shows the corresponding geometry. Regarding the considered dimensions, the HTF part is implemented one-dimensionally in the z-direction, and the PCM part two-dimensionally in the z- and the r-direction. Both parts are coupled via an interface, which contains the wall properties. In the sketch r_{eff} is the effective storage radius.

2.2.2. Assumptions for the numerical model

FASTER is tailored to simulate the heat transfer processes in large-scale LH-TES efficiently. This is achieved by the following simplifications of the physics [37].

1) Quasi-steady-state HTF flow: The processes in the HTF are much faster than the processes in the PCM which results in HTF equilibrium states for every PCM state.
2) 1D simulation of the HTF: No resolution of the HTF state in the radial direction.
3) Thermodynamic equilibrium in the HTF: It is assumed that the thermodynamic steam fraction is the actual steam fraction.
4) An effective fin model to represent the PCM/fin part of the storage is used, described in detail in [37].

Assumption 4 simplifies the thermal behaviour of the storage material considerably. In addition to calibrating the model on the basis of simulations of the cross section in Fluent®, experimental validation is therefore required for reliable quantitative results. Experimental data is currently being collected for this purpose.

2.2.3. Mathematical formulation of the numerical model

On the HTF-side, the first characteristic equation used is the equation of conservation of mass

$$\frac{\partial G_{\mathrm{HTF}}}{\partial z} = 0, \tag{4}$$

with the mass flux G_{HTF} and the axial coordinate of the tube z. Secondly, the equation of conservation of momentum

$$\frac{\partial \mathrm{p}_{\mathrm{HTF}}}{\partial z} = \left(\frac{\partial \mathrm{p}_{\mathrm{HTF}}}{\partial z}\right)_{\mathrm{A}} + \left(\frac{\partial \mathrm{p}_{\mathrm{HTF}}}{\partial z}\right)_{\mathrm{G}} + \left(\frac{\partial \mathrm{p}_{\mathrm{HTF}}}{\partial z}\right)_{\mathrm{F}} \tag{5}$$

with the HTF pressure drops due to acceleration A, gravity G and friction F is implemented. The third characteristic equation is the equation of conservation of energy

$$\mathrm{G}_{\mathrm{HTF}}\frac{\partial \mathrm{h}_{\mathrm{HTF}}}{\partial z} = \frac{\dot{q}_w \mathrm{A}_w}{\mathrm{V}_{\mathrm{HTF}}} \tag{6}$$

with the specific enthalpy of the HTF h_{HTF}, the heat flux across the tube wall $\dot{q}_w$, the wall surface area A_{w} and the volume of the HTF V_{HTF}.

In the following, the constitutive equations of the model are introduced. The calculation of the volumetric steam fraction for boiling based on the heterogenous flow model is

$$\alpha_{\mathrm{HTF}} = \frac{\alpha_{\mathrm{HTF,H}}}{\mathrm{C}_0 + \frac{v_{\mathrm{HTF,vap,j}}}{j_{\mathrm{HTF}}}} \tag{7}$$

with the heterogenous void fraction α_{HTF}, the homogenous void fraction $\alpha_{\mathrm{HTF,H}}$, the distribution coefficient C_0, the drift velocity $v_{\mathrm{HTF,vap,j}}$ and the volume flux j_{HTF}. For condensation,

$$\alpha_{\mathrm{HTF}} = \left(1 - \frac{2\delta_{\mathrm{HTF}}}{d_{\mathrm{tube}}}\right)^2 \tag{8}$$

is used with the condensation film thickness δ_{HTF} and the tube diameter d_{tube}. The frictional pressure drop is described by the Darcy-Weisbach equation for single-phase flow and by the Müller-Steinhagen and Heck correlation for two-phase flow.

A sum of the forced convection heat flux (FC), the boiling heat flux (B) and the condensation heat flux (C) describes the total transferrable heat flux

$$\dot{\mathrm{q}} = \dot{\mathrm{q}}_{\mathrm{FC}} + \dot{\mathrm{q}}_{\mathrm{B}} + \dot{\mathrm{q}}_{\mathrm{C}} \tag{9}$$

and the forced convection Nusselt number is thereby calculated by the Dittus-Boelter equation

$$\mathrm{Nu}_{\mathrm{t}} = 0.023 Re^{0.8} Pr^{\mathrm{n}} \tag{10}$$

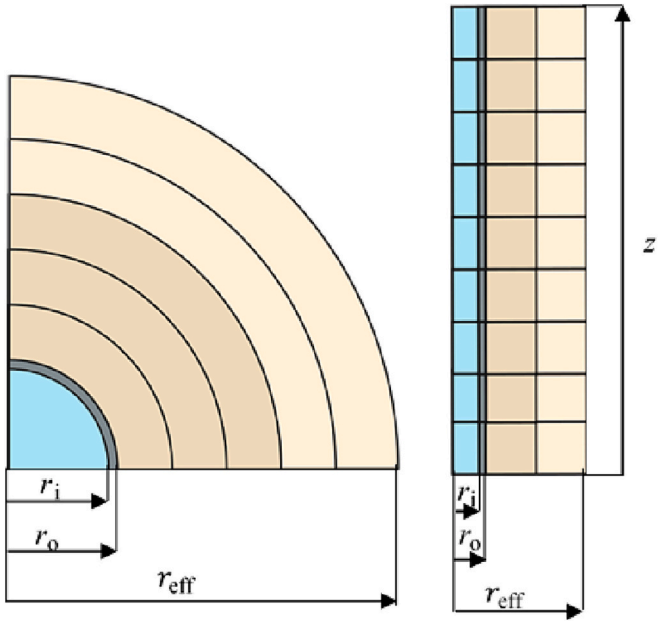

Fig. 2. Illustration of cross-sectional and longitudinal model geometry for the numerical model [37].

with $n = 0.4$ for heating and $n = 0.3$ for cooling.

On the storage side, an effective fin model approximates a homogeneous storage material. Furthermore, the energy equation is transformed for the specific storage enthalpy using the enthalpy porosity method to

$$\rho_{\mathrm{stor}}\frac{\partial h_{\mathrm{stor}}}{\partial t} - \nabla(\lambda_{\mathrm{stor}}\nabla T_{\mathrm{stor}}) = \frac{S_{\mathrm{stor,b}}}{V_{\mathrm{stor}}} + S_{\mathrm{stor,pc}} \tag{11}$$

with the density of the storage ρ_{stor}, the time t, the specific enthalpy h_{stor}, the thermal conductivity λ_{stor}, the temperature T_{stor} and the Volume V_{stor} of the storage, the boundary source term $S_{\mathrm{stor,b}}$ and the source term for phase change $S_{\mathrm{stor,pc}}$.

In the model, the liquid fraction f is defined by the storage temperature related to the solidus temperature T_{sol} and the liquidus temperature T_{liq} of the PCM:

$$f = \begin{cases} 0, T_{\mathrm{stor}} \leq T_{\mathrm{PCM,sol}} \\ 0 \ldots 1, T_{\mathrm{PCM,sol}} < T_{\mathrm{stor}} < T_{\mathrm{PCM,liq}} \\ 1, T_{\mathrm{stor}} \geq T_{\mathrm{PCM,liq}} \end{cases} \tag{12}$$

Further Details on the mathematical formulation of the model can be found in the original publication [37].

2.3. Base cases for the analytical and the numerical model

The analytical parameter study is performed using the standard data set in Table 2. The basis for the values shown are the conditions in an experimental test rig which is currently being operated at DLR. The element has a nominal thermal power of 1 kW, uses the commercial PCM PLUSICE A133 as storage material and can be charged with steam and discharged with water. The water temperatures are assumed in a range of 98 °C and 163 °C, the pressures between 1.2 bar and 6.7 bar, and the mass flow rates between 1.26 kg/h and 1.44 kg/h.

The method for generating the so-called base case consists of the following steps:

Table 2
Comparison of base case values for the analytical and for the numerical study.

	Units	Analytical charging/ discharging	Numerical charging/ discharging
Geometry			
b	–	0.1795	
d_{i}	m	0.0126	
d_{o}	m	0.0172	
L	m	1.5	
s_{PCM}	m	0 or 0.03	Transient
Material properties			
$c_{\mathrm{p,PCM,l}}$	J/(kg K)		2800
$c_{\mathrm{p,PCM,s}}$	J/(kg K)		3200
$T_{\mathrm{PCM,liq}}$	K		412.15/388.15
$T_{\mathrm{PCM,pc}}$	K	407.15/381.15	
$T_{\mathrm{PCM,sol}}$	K		398.15/373.15
$\Delta h_{\mathrm{PCM,sl}}$	J/kg		180000
λ_{fins}	W/ (m^2K)	210	
$\lambda_{\mathrm{PCM,l}}$	W/(mK)	0.214	
$\lambda_{\mathrm{PCM,s}}$	W/(mK)	0.28	
λ_{w}	W/(mK)	42.5	
Operating parameters			
a_{PCZ}	–	1	Transient
$h_{\mathrm{HTF/w}}$	J/kg	7000/11600	
$\dot{m}_{\mathrm{HTF}}$	g/s	0.40/0.35	
$T_{\mathrm{HTF,in}}$	K	437.15/351.15	417.15/368.15
$x_{\mathrm{HTF,in}}$	–	1/0	
$x_{\mathrm{HTF,out}}$	–	0/1	$x_{\mathrm{HTF,out}}$

1) Define geometry-related, material-related and operation-related parameters corresponding to the experimental test rig.
2) Set values for the transient parameter PCM layer thickness to s_{PCM}=0, as for this state the maximum thermal power is expected.
3) Set transient parameters (share of HTF phase change zone and outlet steam quantity) to values for which maximum thermal power is expected.

Besides the presentation of the above method, the following information supports the correct interpretation of Table 2, which contains the values for all constants and variables used in the models. The values for the HTC $h_{\mathrm{HTF/w}}$, the HTF mass flow rate $\dot{m}_{\mathrm{HTF}}$ and the HTF inlet temperature $T_{\mathrm{HTF,in}}$ are different for the charging process in comparison to the discharging process. Furthermore, the share of the HTF phase change zone a_{PCZ}, the distance between the outer tube wall and the phase change boundary of the PCM s_{PCM} and the HTF outlet steam quantity $x_{\mathrm{HTF,out}}$ differ at different points in time. As the analytical model does not take the transience of the processes into account, this has to be simulated using several steady-state test cases. They are generated by assigning fixed values to the transient parameters for different points in time. For the case representing the beginning of the charging/discharging process, the values in the data set for the analytical model are

- 1 for the share of the HTF phase change zone
- 0 m for the distance between the outer tube wall and the phase change boundary of the PCM
- and 1/0 during charging/discharging for the inlet steam quantity respectively.

While the share of the HTF phase change zone and the outlet steam quantity are assumed to be constant during the process, the maximum distance between the outer tube wall and the phase change zone in the PCM is 0.03 m and represents the final state of the process. This corresponds to a state where 3/4 of the total volume of the storage has changed its phase.

The corresponding parameters for the numerical model are listed in Table 2 for comparison. Additional values of the more detailed model are:

- The PCM solidus temperature $T_{\mathrm{PCM,sol}}$ and liquidus temperature $T_{\mathrm{PCM,liq}}$
- The phase change enthalpy of the PCM $\Delta h_{\mathrm{PCM,sl}}$
- The specific heat capacities of the PCM in liquid and solid state $c_{\mathrm{p,PCM,l}}$ and $c_{\mathrm{p,PCM,s}}$

For both models, the definitions for the charging process and the discharging process are as follows:

- Charging implies that the PCM between the outer tube wall and the phase change boundary in the PCM is liquid and $T_{\mathrm{HTF}} > T_{\mathrm{PCM,pc}}$
- Discharging implies that the PCM between the outer tube wall and the phase change boundary in the PCM is solid and $T_{\mathrm{HTF}} < T_{\mathrm{PCM,pc}}$

Starting from the base cases, parameter variations are performed using generic parameter values in a significant range for the analytical model and parameter values within the possibilities for the planned experimental test rig in the numerical model as presented in Sections 3.1 and 3.2.

3. Modelling results

In this section, the results of the analytical and the numerical parameter study will be discussed each with a different focus. The respective objectives of the studies are described in Section 3.1. for the analytical model and in Section 3.2 for the numerical model.

3.1. Analytical results

The key characteristic of PCM storage power is its transient behaviour. When using two-phase HTFs, the distance between the outer tube wall and the phase change boundary of the PCM as well as the HTC between the HTF flow and the inner tube wall vary significantly over time. Their contribution to the overall heat transfer resistance therefore fluctuates. As a result, the respective limiting effect on the overall heat flow rate can change in time and axial location. To show this behaviour systematically, these two parameters are included in the analytical study. An indirect operating parameter, the DHTS, is derived from the findings which can be adjusted most effectively by changing the HTF mass flow rate. This works in a limited mass flow range - an effect that is demonstrated with the help of mass flow rate variation studies. The discharging thermal power is mirrored on the x-axis for better comparability with the charging thermal power in Figs. 3 and 4. If applicable, the base values of the varied parameters from Table 2 are marked with vertical lines in the diagrams. As described in detail in Section 2.1.3, the maximum transferrable thermal power of the LH-TES is estimated by determining the theoretical thermal power that can be transported by the HTF and the theoretical thermal power that can be dissipated radially in the storage under the assumption that the smaller value corresponds to the total thermal power of the storage.

3.1.1. Variation of the distance between the outer tube wall and the PCM phase change boundary

The first investigation deals with the distance between the outer tube wall and the PCM phase change boundary (Eq. (2), curved bracket 3), which determines the thermal resistance due to the PCM layer and contributes to the total *radial heat transfer resistance (HTR)* as can be seen in Eq. (2). In Fig. 3 on the left hand-side, the distance is varied to determine on the one hand its influence on the total HTR and on the other hand the distance at which power control by the mass flow rate becomes possible for each of the three mass flow rates shown. In practice, this knowledge provides information on the duration of a mass-flow-rate-controlled charging/discharging process provided that the transient progression of the PCM layer thickness is known.

In Fig. 3 on the left hand-side, in the first place, the thermal power limited by the radial HTR is shown versus the distance between the outer tube wall and the phase change boundary in the PCM during charging (red solid line) and during discharging (blue solid line). Furthermore, the thermal power limited by the heat capacity of the HTF is illustrated for a mass flow rate of 4.30 g/s, 2.50 g/s and 0.35 g/s (green dashed lines).

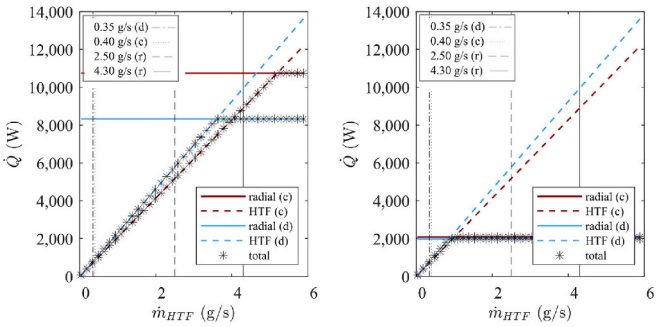

Fig. 4. $\dot{Q}\left(\dot{m}_{HTF}\right)$ limited by radial HTR (solid lines) and by HTF (dashed lines) during charging (c) and discharging (d) as well as total power of the storage for $s_{PCM} = 0$ (left) and for $s_{PCM} = s_{max}$ (right).

It is observed that with increasing distance between the outer tube wall and the PCM phase change boundary, the thermal power limited by radial HTR decreases. For small distances, slightly higher values are reached for the thermal power during charging compared to during discharging. Both profiles converge as the distance grows. The reason for that is the effect of the higher HTC of 11600 W/(m^{2}K) during charging compared to the lower one of 7000 W/(m^{2}K) during discharging. The resulting difference in the HTR between the HTF flow and the inner tube wall leads to a higher thermal power for the charging case. In conclusion, the effect of the HTC between HTF flow and the inner tube wall and the distance between the outer tube wall and the phase change boundary of the PCM are in inverse relation and their effect on the total HTR is correlated, as illustrated by Eq. (2).

Furthermore, the constant thermal power is limited by the HTF

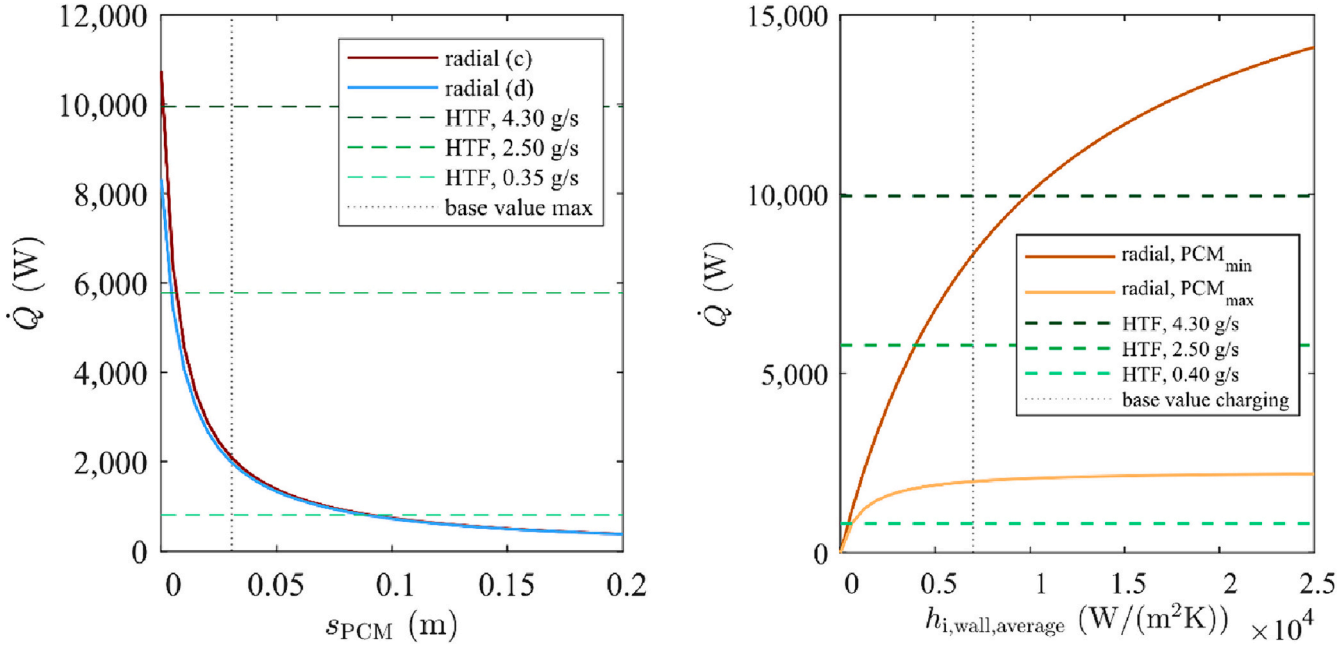

Fig. 3. Left: $\dot{Q}(s_{PCM})$ limited by radial HTR (solid lines) and by HTF (dashed lines) for different $\dot{m}_{HTF}$ during charging (c) and discharging (d). Right: $\dot{Q}(h_{HTF/w})$ limited by radial HTR (solid lines) for minimum and maximum distance between outer tube wall and phase change boundary of the PCM and limited by HTF (dashed lines) for different $\dot{m}_{HTF}$ during charging (equal for discharging).

capacity for different distances. It is 9950 W for 4.30 g/s, 5780 W for 2.50 g/s and 810 W for 0.35 g/s. These values apply to the charging and the discharging process. From the intersections of the radial thermal power with each of the HTF thermal power profiles in Fig. 3 in the left diagram it can be derived that the thermal power of the storage is limited by the HTF heat capacity for distances smaller than 0.1 mm, 0.6 mm and 90.0 mm in the charging case and 0.4 mm and 90.0 mm in the discharging case. Overall, these points indicate, where thermal power control by mass flow rate can be applied during operation and therefore can be considered in the design. This method can generally be applied to storage systems with single-phase HTF flow as well as to systems with two-phase flow.

3.1.2. Variation of the HTC between HTF flow and tube wall

This second Section deals with the investigation of the HTC between HTF flow and tube wall (Eq. (2), curved bracket 1), which defines the thermal resistance due to phase change inside the tube. As indicated in the previous chapter, the distance between the outer tube wall and the phase change boundary in the storage also contributes to the total HTR.

In Fig. 3 on the right-hand-side, the thermal power limited by the radial HTR (solid lines) is shown during charging as a function of the HTC of the two-phase fluid for the maximum as well as for the minimum distance between the outer tube wall and the phase change boundary of the PCM. It increases with increasing HTC for both cases. The increase for the maximum distance stagnates at a thermal power value of 2200 W (light orange solid line) while without any distance in contrast, it continues to >14,100 W (dark orange solid line). This implies that the HTC only becomes relevant for small distances and thus supports the results of Section 3.1.1. For these cases, the operation with two-phase HTFs is especially interesting. Two-phase flows result in high HTCs, in this case, 7000 W/(m^{2}K) during charging and 11600 W/(m^{2}K) during discharging, compared to single-phase flows with values below 50 W/(m^{2}K). Exploiting this significant difference, the heat exchanger tubes in the storage can be divided into a high-power area where the phase change of the HTF occurs and a low-power area, where the single-phase HTF is flowing. The adjustment of the size of the high-power area, the DHTS, can be utilised as an indirect operating parameter. Its potential and the ways of adapting it using conventional design and operating parameters are analysed in detail in Section 3.2.

The results from Sections 3.1.1 and 3.1.2 show that, depending on the system, the operating mode and the time under consideration, the HTC between the flow and the inner tube wall can become limiting for the heat transfer. This implies that, where the HTF phase change occurs, most of the total energy is transferred due to the significantly higher HTCs in these two-phase areas. The indirect operating parameter DHTS can be derived. Changing the mass flow rate is the most effective method for adjusting this DHTS without changing the capacity of the storage. This works in the limited mass flow range in which the thermal power dissipated by the HTF is lower than the thermal power transmitted radially in the storage, an effect that can be seen from the previous study in this section and which is investigated in more detail in the following study on varying mass flow rates in Sections 3.1.3 and 3.1.4.

3.1.3. Variation of HTF mass flow rate for boundary case with minimum PCM layer thickness

This Section deals with the investigation of the HTF mass flow rate (Eq. (1)), which determines the thermal power that can be discharged by the HTF based on the phase change enthalpy of the HTF. The boundary case with minimum distance between the outer tube wall and the phase change boundary in the PCM $s_{PCM} = 0$ m during charging and discharging is considered. This corresponds to the beginning of the charging/discharging process when the PCM is fully solid/liquid.

In the left diagram in Fig. 4, the thermal power limited by the radial HTR (solid lines) and the one limited by the heat capacity of the HTF (dashed lines) are plotted versus the mass flow rate of the HTF during charging (red) and discharging (blue). To relate the different diagrams of Section 3.1, the vertical lines in Fig. 4 mark the mass flow rates used in Fig. 3.

When looking at the diagram on the left-hand side, it becomes apparent that the thermal power limited by the radial HTR is constant for varying HTF mass flow rates under the assumed conditions. With a value of 10750 W, it is higher during charging compared to 8320 W during discharging. This can be explained by the fact that without any distance between the outer tube wall and the phase change boundary in the PCM, the corresponding part of the overall radial HTR in Eq. (2) in bracket 3 disappears. As a consequence, the effect of the HTC between the HTF flow and the tube in bracket 1 as well as the thermal conductivity of the tube in bracket 2 becomes apparent.

Furthermore, valuable information can be inferred from the intersections of the thermal power limited by the radial HTR and the thermal power limited by the HTF capacity. For mass flow rates below 5 g/s during charging and 4 g/s during discharging, the total thermal power, marked with asterisks in the diagram, is limited by the HTF heat capacity. This means that changes in the radial HTR do not have any effect on the overall thermal power in this case. Thus, the thermal power of the storage can be controlled by the HTF mass flow rate. This insight can have great benefits for practical application. Apart from the fact that the total thermal power of both single-phase and two-phase HTF storage systems can be limited in principle by reducing the mass flow rate, the size of the DHTS can be adjusted additionally in two-phase systems. In cases where the theoretical storage capacity is higher than the theoretical enthalpy flow that can be dissipated via the HTF, the HTF changes phase over a flow distance smaller than the total tube length. As a result, a single-phase area and a two-phase area are formed in the tube. The two-phase area is the DHTS and varies in size depending on the thermal power of the storage compared to the HTF enthalpy flow. For mass flow rates on the right side of the intersection in the left diagram of Fig. 4 on the other hand, the radial HTR becomes limiting and changes in the HTF mass flow rate, and thus in the HTF capacity, do not change the thermal power. In this mass flow rate range, active thermal power control by the HTF mass flow rate is not possible. An LH-TES could only be operated full-load in this mode without any possibility of adjusting the thermal power and thus defining the charging/discharging time.

3.1.4. Variation of HTF mass flow rate for boundary case with maximum PCM layer thickness

Finally, the investigation of the HTF mass flow rate for the boundary case with a maximum distance between the outer tube wall and the phase change boundary in the PCM s_{PCM} =0.03 m is shown in Fig. 4 on the right. While the diagram on the left presents the results for the beginning of the charging/discharging process, this diagram corresponds to the end of the processes when 3/4 of the storage material is liquid/solid.

The thermal power limited by the radial HTR is with 2090 W only slightly higher during charging compared to during discharging with 1950 W. For mass flow rates lower than 1 g/s during both charging and discharging, the thermal power is limited by the heat capacity of the HTF and thus controllable by the HTF mass flow rate. This boundary mass flow rate is by the factor 0.25 respectively 0.28 lower compared to the boundary case with minimum distance between the outer tube wall and the phase change boundary of the PCM. In conclusion, thermal power control by the HTF mass flow rate can be realised for a broad mass flow rate range for small distances between the outer tube wall and the phase change boundary of the PCM. This is the case when the storage geometry prevents large distances and at times close to the initiation of the charging/discharging process. Thermal power control for large distances is possible, but only applicable for small HTF mass flow rate ranges.

3.2. Numerical results

In Section 3.1.2, the DHTS was derived, in Sections 3.1.3 and 3.1.4,

possible effects of the HTF mass flow rate on this indirect operating parameter were demonstrated. This chapter visualises and analyses the potential of the DHTS and the possibilities of its adaptation using the conventional operating, the parameters HTF mass flow rate and temperature difference between the inlet temperature of the HTF and the PCM melting temperature, in more detail. The charging process is usually more flexible, as the HTF at the storage outlet does not have to meet specific criteria in the case of thermal charging. In this article, the focus is therefore on the discharging process.

3.2.1. *Mass flow rate variation for the discharging process*

The first quantity to be investigated as an operating parameter in this Section is the HTF mass flow rate. For this purpose, Fig. 5 shows the profile of the discharging thermal power versus time. While the mass flow rate of the HTF is varied from 0.18 g/s to almost full load operation with 0.7 g/s, the temperature difference between the HTF inlet temperature and the phase change temperature of the PCM of 5 K as well as the tube length of 1.5 m are kept constant. This results in equal integrals for all three cases under the respective thermal power profile.

At the beginning of the discharging process, plateaus of thermal power with different lengths appear. For a mass flow rate of 0.70 g/s 1610 W, for a mass flow rate of 0.35 g/s 810 W and a mass flow rate of 0.18 g/s 410 W are reached. During the plateau, the thermal power decreases with small gradients of 0.08 W/s, 0.01 W/s and <0.01 W/s until the thermal power falls sharply after 300 s, 1020 s and 2400 s respectively. At these points in time, 42 %, 72 % and 85 % of the total storage heat has already been released for the three cases shown. This means that the thermal power of the storage doubles when the mass flow rate is increased from 0.18 g/s to 0.35 g/s and doubles once more when the mass flow rate is doubled again to almost full load operation. The thermal power plateau, referring to the discharging time at constant thermal power output, is 240 % higher at the first doubling and 135 % at the second doubling of the mass flow rate compared to the lowest mass flow rate. In Fig. 5 the vertical lines mark times corresponding to the columns in Fig. 6. Each column is a point in time, here 60 s, 300 s and 2460 s after the initiation of the discharging process.

The first row shows the simulation results for a mass flow rate of 0.18 g/s, which is the lowest mass flow rate in Fig. 6. In the second row, the results for 0.70 g/s are depicted, which is the highest mass flow rate

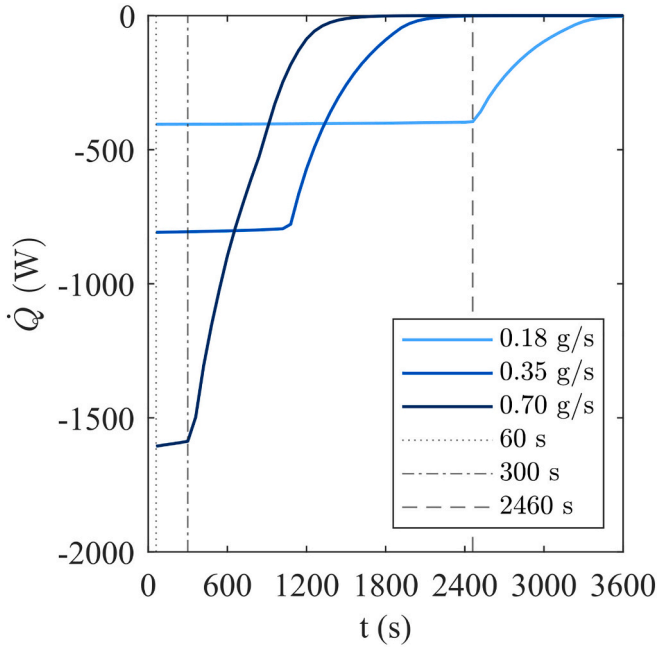

Fig. 5. Thermal power versus time for different HTF mass flow rates and points in time for storage and HTF states in Fig. 6.

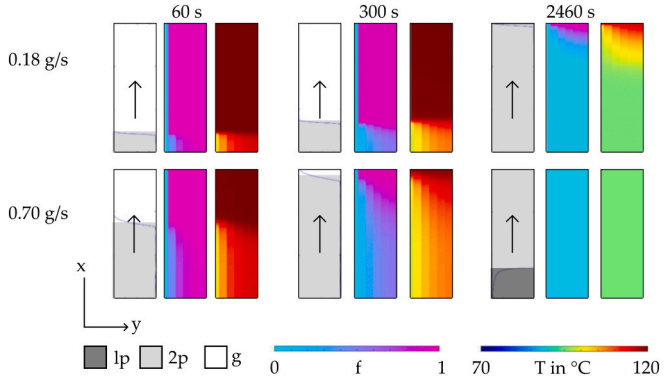

Fig. 6. State of the HTF in the tube, liquid fraction in the storage and temperature in the storage (left to right graphic) at three points in time (left to right column) and for a low and a high HTF mass flow rate (top to bottom).

in the same figure. Every dataset contains on the left hand-side the flow conditions in the HTF tube - either liquid (l), two-phase (2p) or gaseous (g). In the middle, the liquid fraction in the storage (f) and on the right hand-side the temperature fields in the storage are displayed.

In this case, after 60 s, the fluid flow entering the storage tubes from the bottom evaporates over a tube length of approximately 16 % of the total length and then continues flowing up in a gaseous state for a mass flow rate of 0.18 g/s. For a mass flow rate of 0.70 g/s, approximately 58 % of the length is used for evaporation. The reason for this behaviour is the smaller HTF capacity for smaller mass flow rates which limits the total transferrable thermal power and results in the HTF being evaporated after only a short flow path. The HTC between the HTF and the inner tube wall in the forced convection gas zone below 50 W/(m^{2}K), calculated by an adapted version of the Dittus-Bölter equation as described in [37], bounds the evaporation zone. This evaporation zone has been introduced in Section 3.1.2 as DHTS. For the DHTS itself, however, an HTC of 7000 W/(m^{2}K) is assumed based on table values [38]. While the HTF is flowing through the tube from the bottom, the PCM starts to solidify, beginning at the bottom tube inlet. For a mass flow rate of 0.18 g/s, the solidification zone in the storage is shorter after 60 s compared to the solidification zone for a mass flow rate of 0.70 g/s. Also, the temperature decreases in a short area of the storage next to the tube for a mass flow rate of 0.18 g/s while for a mass flow rate of 0.70 g/s, the temperature decrease extends over a long area. This is a direct consequence of the length of the DHTS inside the tube as described in the paragraph above: A shorter DHTS results in a shorter solidification section. After 300 s, the conditions for HTF flow and storage are visualised in the second column of Fig. 6. For a mass flow rate of 0.70 g/s, evaporation occurs over almost the full tube length while for a mass flow rate of 0.18 g/s, approximately 25 % of the tube length is used and gaseous HTF fills the rest of the tube. The solidification process happens over almost the full tube length in a radial direction for a mass flow rate of 0.70 g/s. However, the simulation results for a mass flow rate of 0.18 g/s show a melting front moving in the axial direction, starting from the bottom inlet. The temperature field behaves accordingly. Fig. 5 shows on the one hand that the thermal power for a mass flow rate of 0.18 g/s after 300 s continues to decrease moderately with a thermal power change rate <0.01 W/s, at that time the thermal power plateau is stable. For this case, 80 % of the tube length is still free from solidified PCM and can be used for radial heat transfer under low heat resistance conditions. For a mass flow rate of 0.70 g/s on the other hand, the thermal power drops with a thermal power change rate of 2.36 W/s. The complete outer tube surface is covered with solidified PCM which inhibits the radial heat transfer and hence inhibits the transferable thermal power.

2460 s after the initiation of the discharging process, for both mass flow rates, the entering liquid can be evaporated only partly before leaving the tube as the storage is already discharged to a large extent.

For a mass flow rate of 0.18 g/s two-phase flow fills the whole tube and 12 % of the PCM in the storage are still liquid in the upper part of the storage. A temperature gradient is visible accordingly and sensible heat can still be stored. For a mass flow rate of 0.70 g/s, approximately 25 % of the tube close to the inlet are filled with liquid. All the PCM is solid and a steady state has been established in the storage, its temperature has reached HTF inlet temperature. As expected, the higher discharging thermal power for larger mass flow rates results in shorter discharging time.

In summary, the storage discharging thermal power is proportional to the HTF mass flow rate and the discharging time consequently decreases with increasing mass flow rates/thermal powers. The main reason for this is the limitation of the thermal power of the storage by the HTF capacity which defines the size of the DHTS. Larger two-phase zones and consequently larger DHTSs result in higher thermal powers. Small DHTS are accompanied by axial discharging behaviour, while large ones result in radial discharging around the storage tube. This shows that the mass flow rate can be effectively used to adjust the DHTS as an indirect operating parameter.

3.2.2. *Temperature variation for the discharging process*

The second quantity to be investigated in the numerical study is the HTF inlet temperature. Fig. 7 shows the profile of the discharging thermal power versus time. While the temperature difference between the HTF inlet temperature and the PCM phase change temperature is varied, the mass flow rate of 0.35 g/s as well as the tube length of 1.5 m are kept constant.

At the beginning of the discharging process, a peak thermal power of 850 W for a temperature difference of 30 K, 820 W for a temperature difference of 10 K and 810 W for a temperature difference of 5 K is reached. This power decreases with gradients of 0.02 W/s, 0.01 W/s and 0.01 W/s during the plateau, until the thermal power falls sharply after 1020 s, 1200 s and 1680 s with slopes of 1.27 W/s, 1.50 W/s and 2.04 W/s respectively. The latter slopes are calculated between the starting time of the drop for a duration of 240 s.

This shows that an increased temperature difference results in increased thermal power of the storage by 1 % when it is increased from 5 K to 10 K and a further 4 % when it is increased again from 10 K to 30 K. The thermal power plateau, referring to the discharging time at constant thermal power, is extended by 18 % for a 10 K increase and 40 % for a 30 K increase compared to the smallest temperature difference.

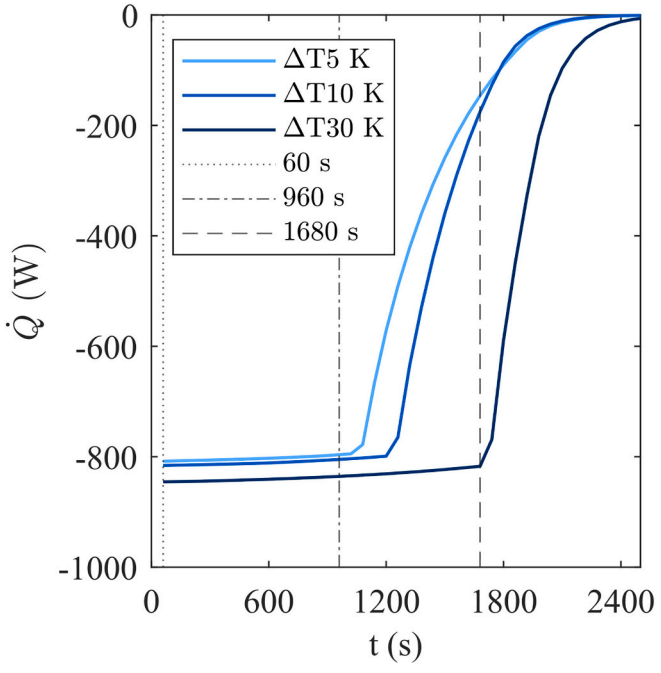

Fig. 7. Thermal power versus time for different temperature differences between the HTF inlet temperature and the phase change temperature of the PCM.

In analogy to the results for the mass flow rate variation in Section 3.2.1, the local discharging behaviour in the storage changes for temperature difference variations. In this case, the size of the two-phase area inside the tube, which represents the DHTS and can be seen in Fig. 8, is larger for a temperature difference of 5 K compared to 30 K. The larger driving temperature difference enhances the radial temperature gradient and thermal discharging power and thus shortens the length of the flow path that is necessary to evaporate the HTF. For the reasons given in Section 3.2.1, this results in an axial discharging behaviour for the smaller evaporation surface and a radial discharging behaviour for the larger evaporation surface. Furthermore, the total transferrable amount of energy increases with increased temperature difference between the HTF inlet temperature and the phase change temperature of the PCM as more sensible heat can be discharged. For a temperature difference of 5 K, approximately 10 % of the total dischargeable heat can be stored sensibly, for 10 K 19 % and for 30 K 43 %. This is why the integral under the thermal power profiles becomes smaller with decreasing temperature differences.

In conclusion, an increase in temperature difference between the HTF inlet temperature and the phase change temperature of the PCM has two effects: An increase in the peak thermal power and an increase in the amount of dischargeable heat due to increased sensible share. Thus, the size of the DHTS is less sensitive to the temperature difference than to the mass flow rate. Also, the rise in temperature and pressure of the steam produced can be a disadvantage for the customer. Furthermore, the solidification area in the storage shortens and widens and the radial temperature gradient increases.

4. Discussion

The two models presented in this article serve different purposes and cannot be directly compared. While the analytical model introduces the idea of the HTC as an HTF-side parameter affecting thermal power of the storage and how it can be utilised for alternative thermal storage power control, the numerical model demonstrates how the indirect operating parameter DHTS can be practically integrated into the operation of a real storage system based on conventional operating parameters.

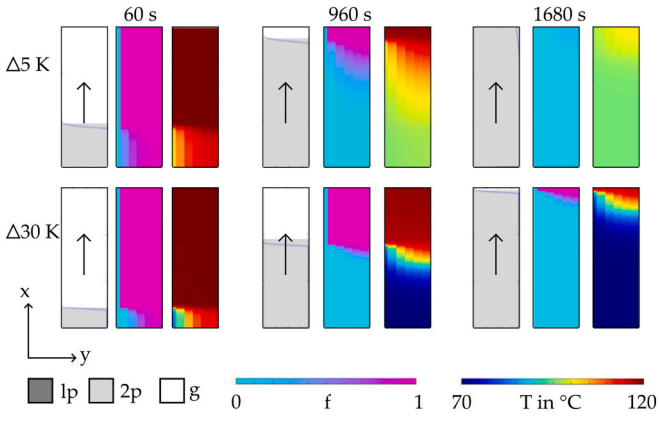

Fig. 8. State of the HTF in the tube, liquid fraction in the storage and temperature in the storage (left to right graphic) at three points in time (left to right column) and for a low and a high-temperature difference between the inlet temperature of the HTF and the phase change temperature of the PCM (top to bottom).

4.1.1. Discussion of analytical results: the DHTS as an indirect operating parameter

The aim of the analytical investigation is to show the interaction of the transient parameters with their effect on the total radial heat transfer resistance and thus on the resulting thermal storage capacity. Additionally, it introduces an indirect operating parameter and its adjustment possibilities. It reveals the effects of the main transient factors on the total thermal power of passive LH-TES: The distance between the outer tube wall and the phase change boundary, the HTC between the HTF flow and the inner tube wall as well as the HTF mass flow rate. While the first and second parameters influence the achievable radial thermal power, the third parameter affects the thermal power, which can be removed by the HTF flow. The limiting effect of the parameters increases for decreasing HTF mass flow rates, increasing distance between the outer tube wall and the phase change boundary and decreasing HTC. It is demonstrated that depending on the system, at times and locally, besides the PCM layer, the HTC controls the thermal power of the storage. The DHTS can be derived from this finding to extend the conventional operating parameters. It can be set most precisely using the HTF mass flow rate in cases where the mass flow rate limits the thermal power of the storage. For small distances between the outer tube wall and the phase change boundary in the PCM, the mass flow rate range, in which thermal storage power control is possible, is wider than for large distances. Obviously, the analytical model is simplified. However, it serves to illustrate the interaction between the effects caused by the growing PCM layer and the changing HTC as well as the adjustment mechanism of the DHTS using the mass flow rate of the HTF.

4.1.2. Discussion of the numerical results: setting the DHTS

While in the analytical model, the HTF side and the storage side of the system are not coupled directly and the total thermal power is determined by comparing the theoretical maximum thermal powers of both sides, the numerical model additionally considers their interaction and thus is suitable for storage design purposes. The goal of the study is to show, how the conventional design parameters can be used to adjust the indirect operating parameter DHTS. In this way, it is possible to determine which combination of geometrical, material and operating parameters is suitable for achieving the required performance. Operating strategies where only parts of the full tube length are used for the phase change of the HTF offer peak-shaved thermal power characteristics with extended charging and discharging times and lead to axial charging/discharging behaviour. The size of the DHTS can hereby be defined in the design process combining the inlet HTF temperature and the HTF mass flow rate as operating parameters as well as the tube length as geometric parameter. Increasing the inlet temperature enhances thereby capacity and charging/discharging time for the reasons discussed in Section 3.2.2. Extending the tube length has the same effect for a different reason: Longer tubes result in larger storages with more capacity. The only parameter for thermal storage power control which does not lead to changes in storage capacity is therefore the mass flow rate. However, the actual flexibility of the above-discussed parameters during operation is different. While the mass flow rate can be varied in a range within the boundaries of the system, the flexibility of the HTF inlet temperature is limited by the melting temperature of the PCM and the tube length is not flexible after initial fabrication of the storage. Only the number of HTF tubes can be increased in modular storage systems by retrofitting the storage unit. The extent to which the use of the proposed operating strategy is economically advantageous depends on whether the overall system can be simplified by using a larger storage unit that is only operated at partial load, thereby reducing costs. For example, it could replace several smaller storages with associated pipe systems, valves and pumps, which are discharged in sequence to extend the discharging time of the overall system.

5. Conclusions

The analytical study demonstrates, how, in any system, the HTC controls not only the temporal, but also the spatial behaviour of the thermal power. Based on this, an indirect operating parameter referred to as the *dominant heat transfer surface* (DHTS) extends the classic operating parameters. This indirect parameter can be set most precisely using the HTF mass flow rate in cases where the mass flow rate limits the thermal power of the storage. The numerical study indicates how, by incorporating the DHTS as a new operating parameter, optimised coupled design and operating strategies can be derived. The resulting thermal power is thereby transferred only in a fraction of the tubes, which leads to a peak shaving behaviour of the storage with defined charging and discharging times.

The results presented in this study show the relevance of the HTF-side operating parameters in LH-TES and the conditions under which they can be used for power control. By implementation of new operating strategies based on these parameters, customised storage design and operation can be enabled.

The basis for the values used in the analytical and numerical model are the conditions of an experimental test rig, which is currently being operated to verify the simulation results. The storage element has a nominal thermal power of 1 kW, uses the commercial PCM PLUSICE A133 with a phase change temperature of 133 °C, and can be charged with steam and discharged with water. The water temperatures can be varied between 98 °C to 163 °C, the pressures between 1.2 bar and 6.7 bar, and the mass flow rates between 1.26 kg/h and 1.44 kg/h.

In future work, the presented numerical simulation model will be validated and used for techno-economic analyses.

CRediT authorship contribution statement

Larissa Dietz: Writing – review & editing, Writing – original draft, Visualization, Methodology, Investigation, Conceptualization. **Inga Bürger:** Writing – review & editing, Supervision, Conceptualization. **Andrea Gutierrez:** Writing – review & editing, Supervision.

Declaration of competing interest

The authors declare that they have no known competing financial interests or personal relationships that could have appeared to influence the work reported in this paper.

Data availability

Data will be made available on request.

References

[1] I. Dincer, M.A. Ezan, Heat Storage: A Unique Solution for Energy Systems, Springer, Cham, 2018.
[2] Q. Li, et al., A review of performance investigation and enhancement of shell and tube thermal energy storage device containing molten salt based phase change materials for medium and high temperature applications, Appl. Energy (2019) 255, https://doi.org/10.1016/j.apenergy.2019.113806.
[3] Y.B. Tao, Y.K. Liu, Y.-L. He, Effects of PCM arrangement and natural convection on charging and discharging performance of shell-and-tube LHS unit, Int. J. Heat Mass Transf. (2017) 115, https://doi.org/10.1016/j.ijheatmasstransfer.2017.07.098.
[4] S.S.M. Tehrani, G. Diarce, R.A. Taylor, The error of neglecting natural convection in high temperature vertical shell-and-tube latent heat thermal energy storage systems, Sol. Energy (2018) 174, https://doi.org/10.1016/j.solener.2018.09.048.
[5] S. Riahi, et al., Performance comparison of latent heat storage systems comprising plate fins with different shell and tube configurations, Appl. Energy (2018) 212, https://doi.org/10.1016/j.apenergy.2017.12.109.
[6] M.D. Muhammad, O. Badr, Performance of a finned, latent-heat storage system for high temperature applications, Appl. Therm. Eng. (2017) 116, https://doi.org/10.1016/j.applthermaleng.2017.02.006.

[7] F. Yuan, et al., Experimental study on thermal performance of high-temperature molten salt cascaded latent heat thermal energy storage system, Int. J. Heat Mass Transf. (2018) 118, https://doi.org/10.1016/j.ijheatmasstransfer.2017.11.024.
[8] J. Sunku Prasad, et al., Comparative study of phase change phenomenon in high temperature cascade latent heat energy storage system using conduction and conduction-convection models, Sol. Energy (2018) 176, https://doi.org/10.1016/j.solener.2018.10.048.
[9] Y. Zhao, et al., Experimental study on the thermodynamic performance of cascaded latent heat storage in the heat charging process, Energy (2018) 157, https://doi.org/10.1016/j.energy.2018.05.193.
[10] C. Li, et al., Heat transfer of composite phase change material modules containing a eutectic carbonate salt for medium and high temperature thermal energy storage applications, Appl. Energy (2019) 238, https://doi.org/10.1016/j.apenergy.2019.01.184.
[11] Y.B. Tao, Y.L. He, Z.G. Qu, Numerical study on performance of molten salt phase change thermal energy storage system with enhanced tubes, Sol. Energy 86 (5) (2012), https://doi.org/10.1016/j.solener.2012.01.004.
[12] H. Qiao, V. Aute, R. Radermachen, Comparison of equation-based and non-equation based approaches for transient modeling of a vapor compression cycle, in: International Refrigeration and Air Conditioning Conference, 2012.
[13] M. Parsazadeh, X. Duan, Numerical and statistical study on melting of nanoparticle enhanced phase change material in a shell-and-tube thermal energy storage system, Appl. Therm. Eng. (2017) 111, https://doi.org/10.1016/j.applthermaleng.2016.09.133.
[14] Y. Cao, A. Faghri, Performance characteristics of a thermal energy storage module: a transient PCM/forced convection conjugate analysis, Int. J. Heat Mass Transf. 34 (1) (1991), https://doi.org/10.1016/0017-9310(91)90177-G.
[15] C. Bellecci, M. Conti, Phase change thermal storage: transient behaviour analysis of a solar receiver/storage module using the enthalpy method, Int. J. Heat Mass Transf. 36 (8) (1993), https://doi.org/10.1016/S0017-9310(05)80146-2.
[16] M. Lacroix, Numerical simulation of a shell-and-tube latent heat thermal energy storage unit, Sol. Energy 50 (4) (1993), https://doi.org/10.1016/0038-092X(93)90029-N.
[17] Y. Zhang, A. Faghri, Semi-analytical solution of thermal energy storage sytem with conjugate laminar forced convection, Int. J. Heat Mass Transf. 39 (4) (1996), https://doi.org/10.1016/0017-9310(95)00172-7.
[18] A. Trp, K. Lenic, B. Frankovic, Analysis of the influence of operating conditions and geometric parameters on heat transfer in water-paraffin shell-and-tube latent thermal energy storage unit, Appl. Therm. Eng. 26 (16) (2006), https://doi.org/10.1016/j.applthermaleng.2006.02.004.
[19] K.A.R. Ismail, M.M. Abugderah, Performance of a thermal storage system of the vertical tube type, Energy Convers. Manag. (1999) 41, https://doi.org/10.1016/S0196-8904(99)00140-5.
[20] C. Zauner, et al., Experimental characterization and simulation of a fin-tube latent heat storage using high density polyethylene as PCM, Appl. Energy (2016) 179, https://doi.org/10.1016/j.apenergy.2016.06.138.
[21] Y. Wang, et al., Experimental study on the melting and solidification behavior of erythritol in a vertical shell-and-tube latent heat thermal storage unit, Int. J. Heat Mass Transf. (2016) 99, https://doi.org/10.1016/j.ijheatmasstransfer.2016.03.125.
[22] H. Niyas, C.R.C. Rao, P. Muthukumar, Performance investigation of a lab-scale latent heat storage prototype – experimental results, Sol. Energy (2017) 155, https://doi.org/10.1016/j.solener.2017.07.044.
[23] A. Bahlekeh, et al., Evaluation of the solidification process in a double-tube latent heat storage unit equipped with circular fins with optimum fin spacing, Energy Sci. Eng. 11 (7) (2023), https://doi.org/10.1002/ese3.1473.
[24] I. Shojaeinasab Chatroudi, et al., Heat transfer enhancement and free convection assessment in a double-tube latent heat storage unit equipped with optimally spaced circular fins: evaluation of the melting process, Front. Energy Res. (2023) 11, https://doi.org/10.3389/fenrg.2023.1097382.
[25] R.E. Murray, D. Groulx, Experimental study of the phase change and energy characteristics inside a cylindrical latent heat energy storage system: part 1 consecutive charging and discharging, Renew. Energy (2014) 62, https://doi.org/10.1016/j.renene.2013.08.007.
[26] A. Sari, K. Kaygusuz, Thermal energy storage system using stearic acid as a phase change material, Sol. Energy 71 (6) (2001), https://doi.org/10.1016/S0038-092X(01)00075-5.
[27] A. Hasan, Phase change material energy storage system employing palmitic acid, Sol. Energy 52 (2) (1994), https://doi.org/10.1016/0038-092X(94)90064-7.
[28] M. Akgün, O. Aydın, K. Kaygusuz, Thermal energy storage performance of paraffin in a novel tube-in-shell system, Appl. Therm. Eng. 28 (5–6) (2008), https://doi.org/10.1016/j.applthermaleng.2007.05.013.
[29] D. Laing, et al., Development of high temperature phase-change-material storages, Appl. Energy (2012) 109, https://doi.org/10.1016/j.apenergy.2012.11.063.
[30] D. Laing, et al., High temperature PCM storage for DSG solar thermal power plants tested in various operating modes of water/steam flow, in: Solar Paces 2012, 2012 (Marrakech, Marokko).
[31] D. Laing, et al., Analysis of operation test results of a high temperature phase change storage for parabolic trough power plants with direct steam generation, in: ASME 6th Conference on Energy Sustainability, 2012 (San Diego).
[32] P. Garcia, M. Olcese, S. Rougé, Experimental and numerical investigation of a pilot scale latent heat thermal energy storage for CSP power plant, Energy Procedia (2015) 69, https://doi.org/10.1016/j.egypro.2015.03.102.
[33] P. Garcia, S. Rougé, P. Nivelon, Second test campaign of a pilot scale latent heat thermal energy storage – durability and operational strategies, in: AIP Conference, American Institute of Physics, 2016.
[34] P. Garcia, et al., Experimental results from a pilot scale latent heat thermal energy storage for DSG power plants – advanced operating strategies, in: SOLARPACES 2020: 26th International Conference on Concentrating Solar Power and Chemical Energy Systems, 2022.
[35] C. Beust, et al., Predictive approach of heat transfer for the modelling of large-scale latent heat storages, Renew. Energy (2020) 157, https://doi.org/10.1016/j.renene.2020.04.135.
[36] M. Johnson, et al., Design of high temperature thermal energy storage for high power levels, Sustain. Cities Soc. (2017) 35, https://doi.org/10.1016/j.scs.2017.09.007.
[37] J. Vogel, M. Keller, M. Johnson, Numerical modeling of large-scale finned tube latent thermal energy storage systems, J. Energy Storage (2020) 29, https://doi.org/10.1016/j.est.2020.101389.
[38] H. Kuchling, Taschenbuch der Physik, Carl Hanser Verlag GmbH & Co. KG, 2010.